Free vibration analysis of a rotating pre-twisted beam subjected to tendon-induced axial loading

V. Ondra[a,*], B. Titurus[a]

[a] *University of Bristol, Department of Aerospace Engineering, University Walk, BS8 1TR Bristol, United Kingdom*

Abstract

The main objective of this paper is to investigate free vibration of a rotating pre-twisted beam with bending-bending-torsion coupling that is axially loaded by a tendon. The tendon is connected to the tip of the beam, passes through its body, and is fixed and loaded at the axis of rotation. Due to their connection, the motion of the beam influences the motion of the tendon and vice versa. The equations of motion of the beam-tendon system are introduced and solved numerically by a combination of a boundary value problem solver and differential quadrature method to obtain the natural frequencies and mode shapes of the system. The numerical implementation is firstly validated against literature for a non-rotating beam-tendon system and a rotating pre-twisted blade. Then, the effect of the tendon on the free vibration of the system is studied for a wide range of loading cases and rotation speeds. From the computed modal characteristics, it is found that the presence of a tendon leads to the frequency shift of beam's natural frequencies as well as frequency loci veering between the beam-dominated and tendon-dominated modes. Both of these effects strongly depend on the beam-tendon rotation speed.

Keywords: beam-tendon system, rotating pre-twisted beam, Campbell diagram, frequency-loading diagram, frequency loci veering

Highlights

- A rotating pre-twisted beam subjected to tendon-induced axial loading is studied
- The coupled beam-tendon system is modelled using partial differential equations
- Free vibration analysis is numerically conducted
- The effect of the tendon on the modal properties is studied for a range of configurations
- The presence of the tendon results in frequency shifts and frequency loci veering

Nomenclature

Symbol	Description
b	Subscript for a boundary
B_1, B_2	Cross-sectional constants, m^5, m^6
d	Subscript for a domain
e	Distance between mass and elastic axes, m
e_A	Distance between tensile and elastic axes, m

*Corresponding author.
Email addresses: vaclav.ondra@bristol.ac.uk (V. Ondra), brano.titurus@bristol.ac.uk (B. Titurus)

f	Natural frequency, Hz
EI_1, EI_2	Flapping and lead-lag rigidities, $\mathrm{N\,m^2}$
GJ	Torsional rigidity, $\mathrm{N\,m^2}$
k_A	Polar radius of gyration of cross-sectional area, m
k_{m1}, k_{m2}	Mass radii of gyration in flapping and lead-lag directions, m
k_m	Polar radius of gyration, m
$\mathbf{K}$	Stiffness matrix
L_y, L_z	External excitation forces in y and z directions, $\mathrm{N\,m^{-1}}$
m	Mass of the blade per unit length, $\mathrm{kg\,m^{-1}}$
m_t	Mass of the tendon per unit length, $\mathrm{kg\,m^{-1}}$
M	External excitation moment about elastic axis (torque), N m
$\mathbf{M}$	Mass matrix
N_x	Number of sampling points
P	Applied tension corresponding to axial force, N
P_cr	Critical force, N
R	Length of the beam and tendon, m
t	Time, s
T, T_t	Centrifugal forces acting on the blade and the tendon, N
U	Potential energy, J
$\mathbf{U}$	Vector of unknown functional values
w, v	Flapping and lead-lag bending displacements of the blade, m
v_t, w_t	Flapping and lead-lag transversal displacements of the tendon, m
$W, V, \Phi, W_\mathrm{t}, V_\mathrm{t}$	Mode shape components of the beam and tendon
W	Work, J
x	Independent spatial variable, m
x_i	Sampled independent spatial variable, m
β	Initial pre-twist angle, rad
ϕ	Torsional displacement, rad
Ψ	Mode shape of the system
ω	Angular natural frequency, $\mathrm{rad\,s^{-1}}$
Ω	Rotor speed, $\mathrm{rad\,s^{-1}}$
$\dot{(\bullet)}$	Partial derivative with respect to time
$(\bullet)'$	Partial derivative with respect to spatial variable
BC	Boundary condition
bvp4c	Boundary value problem solver
DQM	Differential Quadrature Method
F-L	Frequency-loading
ODE	Ordinary differential equation
PDE	Partial differential equation

1. Introduction

It has been recently suggested to investigate an active tendon concept as a means of controlling rotorcraft blade dynamics properties [1]. This concept uses a tendon that is connected to a blade's tip, passes through its whole body and is fixed and loaded at the root of the blade. The applied force, which is transferred by the tendon, axially loads the blade and can therefore influence its dynamic properties [2]. It was shown that by varying the applied load, the dynamic properties of the blade can be modified such that a rotorcraft can operate with a variable rotor speed and/or morphed blades while experiencing no significant loading due to the resonances. The preliminary studies and experimental demonstrations [3–5] conducted so far used simplified models of beam-tendon system with no cross-sectional coupling or pre-twist, and the effect of rotation was only sporadically considered. Therefore, this paper aims to investigate free vibration of an isotropic rotating beam featuring bending-bending-torsion coupling due to an offset of shear and mass centres

and pre-twist, which is coupled to and axially loaded by a tendon. The numerical analysis is conducted using parameters similar to a main rotor blade of a light helicopter so the results can be interpreted in the context of an active tendon concept development.

Modelling of beams and tendons is in general a well established subject which has been extensively studied, because beams and tendons are two essential structural elements that are frequently used in many engineering applications. There is a large number of studies that focus on different aspects of beam and tendon modelling, application and testing [6–9]. The beams are often modelled as straight with no pre-twist as this model represents a wide range of practical applications. However, the lack of pre-twist means that there is no coupling between the two bending directions. Moreover, from a large body of literature [7, 10–14], it is also known that the pre-twist has significant impact on the beam's modal properties. Therefore, to represent a typical rotorcraft blade, the pre-twist must be considered. Many theoretical approaches [9], ranging from classical theories, such as the Euler-Bernoulli theory [15, 16] and Timoshenko theory [17–19], to geometrically-exact, fully intrinsic composite blade theory [8], have been developed for rotating pre-twisted beams that represent rotorcraft blades. Similarly, many applications and theories for tendons (strings, cables), which are often used as a means of actuating and controlling structures, have been investigated [6, 20–23].

However, despite a large number of studies, only a few used a similar configuration to the present beam-tendon system. In [24–26] a tendon was used for vibration control of a simple cantilever beam where it was found that vibration of the beam can be effectively suppressed by applying and releasing the tendon tension in a prescribed matter. As these studies modelled the effect of the tendon using an axial force, the motion of the tendon and its influence on vibration of the beam was not evaluated. The effect of axial loading on the rotating pre-twisted beams and the application for resonance avoidance in rotorcraft have been investigated in [2]. It was observed that the axial load has potential to allow rotorcraft to operate with variable rotor speed without danger of main rotor resonances. However, the effect of the tendon, which is proposed to deliver the axial loading, has not been considered. All the previous studies considered axially loaded beams, arguably because the dynamics of such axially-loaded beams is well understood [27, 28]. In contrast, a string-beam system was modelled in [29] as a representation of an optic cable coupler. However, the axial tension of the string had no influence on the beam so the dynamics of the beam was not coupled with the motion of the tendon. In [4, 5, 30] the coupling between a tendon and a cantilever beam has been considered, but there was no cross-sectional coupling or pre-twist included. Free vibration analysis of beam-tendon system with bending-torsion coupling was also conduced in [3], but the pre-twist was omitted and the effect of rotation only sporadically discussed. To the best knowledge of the authors, there are no studies of rotating, pre-twisted beam-tendon system available in literature. Therefore, the main objective of the paper is to investigate free vibration of such a system. In particular, the effect of the tendon on the natural frequencies of the beam, and the effect of the rotation on the tendon are investigated in detail. The present paper extends previous studies of beam-tendon systems [3–5] by including the effect of rotation, pre-twist and cross-sectional coupling.

The paper is organised as follows: the theoretical model of the system and a numerical procedure used are introduced in section 2. The validation of the numerical implementation against the results previously reported in literature is done in section 3. Then, in section 4, the main numerical results and parametric studies are reported. In particular, it is shown what is the effect of rotation on the minimum and maximum allowed loading forces. These are determined by the need to overcome the centrifugal force, and to avoid stability loss. Then, the difference between the frequency-loading diagram with and without rotation is studied and finally, the Campbell diagram for selected system parameters is computed. In section 5 the main findings and limitations of the study are discussed. The paper is accompanied by three appendixes: in Appendix A the equations of motions are derived using the principle of minimum potential energy, in Appendix B the details of the used boundary value problem solver (bvp4c) are given, and in Appendix C the differential quadrature method (DQM) is presented.

2. Theoretical model and numerical methods

The system under consideration is an isotropic rotating pre-twisted cantilever beam with uniform parameters loaded by a tendon as depicted in Fig. 1. The tendon is attached at the tip of the beam, passes

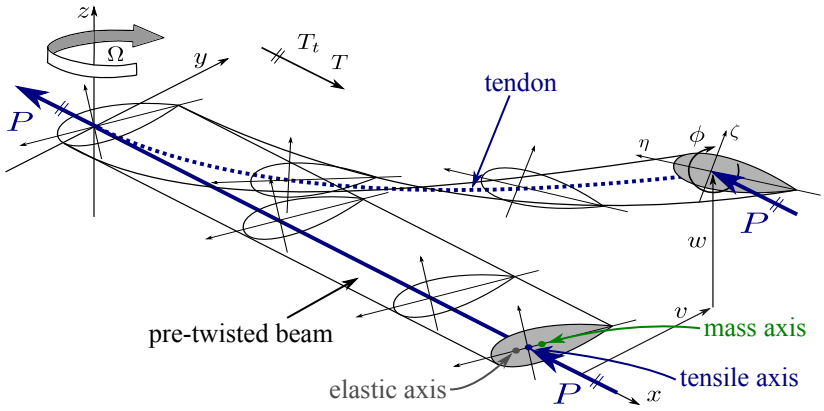

Figure 1: Rotating beam-tendon system consisting of an isotropic, pre-twisted cantilever beam which features an offset between the mass, elastic and tensile axes, and which is subjected to the tendon-induced axial load. The tendon is connected at the tip of the beam, passes freely through its whole body and is fixed and loaded at the axis of rotation.

through its whole body and is fixed and loaded at the axis of rotation. The tendon is free to vibrate inside the beam and, due to an assumption of small deflections, it never collides with its inner surface. The tendon coincides with the tensile axis so that the effect of the tendon on the beam can be modelled as an axial force that is acting against the centrifugal force at the tip at all times. The motion of the beam is described by flapping (bending out-of-plate of rotation) displacement, lead-lag (bending in-plane of rotation) displacement, and torsion about the elastic axis. All three motions are mutually coupled through the cross-sectional offset of elastic and mass axes, and the beam pre-twist. The parameters characterising the beam are uniformly distributed, i.e. they do not vary along the span of the beam, with exception of the pre-twist which linearly changes between the root and the tip. It is assumed that the beam meets all the requirement of the Euler-Bernoulli theory and can therefore be modelled by the linear Houbolt-Brooks equations [15] which are modified to account for the tendon-induced axial loading. The tendon is modelled using the wave equations [20] augmented by the effects of centrifugal forces. Both the beam and the tendon are fixed (clamped) at the axis of rotation, and coupled with each other through the geometrical and loading boundary conditions at the tip. At the tip, their displacements are identical and the tendon-induced axial force contributes to the shear and moment boundary conditions of the blade. Unlike [30], no other connectivity conditions were enforced since the tendon is free to vibrate inside the beam.

2.1. The equations of motion and boundary conditions

The equations of motion and boundary conditions can be derived with the help of the principle of minimum potential energy as detailed in Appendix A. The final partial differential equations (PDEs) describing the system are

$$\frac{\partial^2}{\partial x^2}\Big\{[EI_1\cos^2\beta + EI_2\sin^2\beta]w'' + [EI_2 - EI_1]\sin\beta\cos\beta v'' - Te_A\phi\cos\beta + Pe_A\phi\cos\beta - EB_2\beta'\phi'\sin\beta\Big\}$$
$$- \frac{\partial}{\partial x}\Big\{Tw' - Pw' + \Omega^2 mxe\phi\cos\beta\Big\} + m(\ddot{w} + e\ddot{\phi}\cos\beta) =$$
$$L_z + \frac{\partial^2}{\partial x^2}\Big\{Te_A\sin\beta - Pe_A\sin\beta\Big\} + \frac{\partial}{\partial x}\Big\{\Omega^2 mxe\sin\beta\Big\}, \quad (1a)$$

$$\frac{\partial^2}{\partial x^2}\Big\{[EI_1\sin^2\beta+EI_2\cos^2\beta]v''+[EI_2-EI_1]\cos\beta\sin\beta w''+Te_A\phi\sin\beta-Pe_A\phi\sin\beta-EB_2\beta'\phi'\cos\beta\Big\}$$
$$-\frac{\partial}{\partial x}\Big\{Tv'-Pv'-\Omega^2mxe\phi\sin\beta\Big\}+\Omega^2me\phi\sin\beta+m(\ddot{v}-e\ddot{\phi}\sin\beta)-\Omega^2mv=$$
$$L_y+\frac{\partial^2}{\partial x^2}\Big\{Te_A\cos\beta-Pe_A\cos\beta\Big\}+\frac{\partial}{\partial x}\Big\{\Omega^2mxe\cos\beta\Big\}+\Omega^2m(e_0+e\cos\beta), \quad (1b)$$

$$-\frac{\partial}{\partial x}\Big\{\left[GJ+Tk_A^2-Pk_A^2+EB_1\beta'^2\right]\phi'-EB_2\beta'[v''\cos\beta+w''\sin\beta]\Big\}+Te_A(v''\sin\beta-w''\cos\beta)$$
$$-Pe_A(v''\sin\beta-w''\cos\beta)+\Omega^2mxe(w'\cos\beta-v'\sin\beta)+\Omega^2mev\sin\beta$$
$$+\Omega^2m\left[(k_{m2}^2-k_{m1}^2)\cos2\beta+ee_0\cos\beta\right]\phi+mk_m^2\ddot{\phi}-me(\ddot{v}\sin\beta-\ddot{w}\cos\beta)=$$
$$M+\frac{\partial}{\partial x}\Big\{Tk_A^2\beta'-Pk_A^2\beta'\Big\}-\Omega^2m\left[(k_{m2}^2-k_{m1}^2)\sin\beta\cos\beta+ee_0\sin\beta\right], \quad (1c)$$

$$P\frac{\partial^2 w_{\mathrm{t}}}{\partial x^2}+\frac{\partial}{\partial x}\left(T_{\mathrm{t}}\frac{\partial w_{\mathrm{t}}}{\partial x}\right)-m_{\mathrm{t}}\frac{\partial^2 w_{\mathrm{t}}}{\partial t^2}=0, \quad (1d)$$

$$P\frac{\partial^2 v_{\mathrm{t}}}{\partial x^2}+\frac{\partial}{\partial x}\left(T_{\mathrm{t}}\frac{\partial v_{\mathrm{t}}}{\partial x}\right)-m_{\mathrm{t}}\left(\frac{\partial^2 v_{\mathrm{t}}}{\partial t^2}-\Omega^2 v_{\mathrm{t}}\right)=0, \quad (1e)$$

where $w(t,x)$, $v(t,x)$ are the flapping and lead-lag bending displacements of the blade, $v_{\mathrm{t}}(t,x)$, $w_{\mathrm{t}}(t,x)$ are the flapping and lead-lag transversal displacements of the tendon, $\phi(t,x)$ is the torsional displacement about the elastic axis, t is time, x is the independent spatial variable, EI_1, EI_2 and GJ are the flapping, lead-lag and torsional rigidities, respectively, e is the distance between mass and elastic axes, e_A is the distance between tensile and elastic axes, k_A is the polar radius of gyration of cross-sectional area, k_{m1}, k_{m2} are the mass radii of gyration in flapping and lead-lag directions, respectively, k_m is the polar radius of gyration, B_1, B_2 are cross-sectional constants, m and m_{t} are the mass per unit length of the beam and tendon, respectively, P is the applied loading force which corresponds to the axial force acting on the beam, $\beta(x)$ is linearly varying initial pre-twist angle, Ω is the rotation angular speed, L_y, L_z are the external distributed excitation forces in flapping and lead-lag directions, M is the external excitation moment about the elastic axis (torque), and $(\dot{\bullet})$ and $(\bullet)'$ are partial derivatives with respect to time and spatial variable, respectively. The centrifugal forces acting on the beam T and the tendon T_{t} are defined as

$$T=\Omega^2\int_x^R m\tilde{x}\,\mathrm{d}\tilde{x}, \qquad T_{\mathrm{t}}=\Omega^2\int_x^R m_t\tilde{x}\,\mathrm{d}\tilde{x}, \quad (2)$$

where R in the length of the system. Equations (1a), (1b) and (1c) are very similar to the Houbolt-Brooks equations [15], but the effect of the axial force is included.

The boundary conditions (BCs) must ensure the coupling between the beam and the tendon at the tip. Therefore, at the tip ($x=R$)

$$\{-(EI_1\cos\beta^2+EI_2\sin\beta^2)w''-(EI_2-EI_1)\sin\beta\cos\beta v''+(EB_2\beta'\phi'-Pe_A)\sin\beta-Pe_A\phi\cos\beta\}'$$
$$-Pw'+\Omega^2meR(\sin\beta+\phi\cos\beta)+Pw_t'=0, \quad (3a)$$

$$(EI_1\cos\beta^2+EI_2\sin\beta^2)w''+(EI_2-EI_1)\sin\beta\cos\beta v''+(Pe_A+EB_2\beta'\phi')\sin\beta+Pe_A\phi\cos\beta=0, \quad (3b)$$

$$\{-(EI_2-EI_1)\sin\beta\cos\beta w''-(EI_1\sin\beta^2+EI_2\cos\beta^2)v''-(Pe_A+EB_2\beta'\phi')\cos\beta+Pe_A\phi\sin\beta\}'$$
$$-Pv'+\Omega^2meR(\cos\beta+\phi\sin\beta)+Pv_t'=0, \quad (3c)$$

$$(EI_2-EI_1)\sin\beta\cos\beta w''+(EI_1\sin\beta^2+EI_2\cos\beta^2)v''+(Pe_A+EB_2\beta'\phi')\cos\beta-Pe_A\phi\sin\beta=0, \quad (3d)$$

$$\left[GJ - Pk_A^2 + EB_1\beta'^2\right]\phi' - Pk_A^2\beta' - EB_2\beta'(v''\cos\beta + w''\sin\beta) = 0, \tag{3e}$$

$$w_\mathrm{t} = w + e_A(\sin\beta + \phi\cos\beta), \tag{3f}$$

$$v_\mathrm{t} = v + e_A(\cos\beta - \phi\sin\beta) \tag{3g}$$

and at the fixed end ($x = 0$)

$$w = w' = v = v' = \phi = w_t = v_t = 0. \tag{4}$$

Equations (3a) and (3c) prescribe the shear force equality at the tip, Eqs. (3b) and (3d) represent the moments, and Eqs. (3f) and (3g) enforce the same tip displacements of the beam and the tendon. Due to these coupling conditions, the motion of the beam drives the motion of the tendon which, in turn, influences the beam by applying the axial force. This is the reason for an interaction between the modes of the beam and the tendon.

Equations (1)-(3) create a system of two fourth-order and three second-order partial differential equations with the corresponding number of boundary conditions. All these equations must be solved simultaneously as there is coupling between the motions of the beam and the tendon, and also due to chord-wise asymmetry of the beam's cross-section, pre-twist and the connection condition between the beam and the tendon.

2.2. Numerical free vibration analysis

In order to evaluate the modal properties of the beam-tendon system (the natural frequencies ω and the corresponding mode shapes $\Psi(x) = [W(x), V(x), \Phi(x), W_t(x), V_t(x)]$, where $W(x), V(x), \Phi(x), W_t(x), V_t(x)$ are the components of the mode shape which represent, respectively, the bending in the z and y directions, the rotation about the elastic axis, and the transversal motion of the tendon in the z and y directions), two numerical methods, a boundary value problem solver (bvp4c) and a differential quadrature method (DQM), are used in this paper. Although each of them can be theoretically used separately to obtain the modal properties of the system, it was found that due to a complicated nature of the system, the combination of these two methods, as explained in the following, yields accurate and complete sets of results.

A boundary value problem solver used is a Matlab built-in function called bvp4c [31]. The solver is described in more detail in Appendix B. It utilises a collocation formula and is very versatile allowing solutions of a wide range of boundary value problems to be found. However, it does require a starting guess for each vibration mode. In order to obtain all the vibration modes in the frequency region of interest, a set of sufficiently accurate starting guesses needs to be provided. This is a particular issue for the present beam-tendon system due to a number of coupling mechanisms involved and the richness of results for some loading conditions.

In order to obtain the starting guesses required, several approaches may be used. The starting guesses may be obtained using analytical formulas (if available), extracted from the harmonic analysis of the system as in [2] or, as in the case of the present paper, provided by another numerical method. In this study, the differential quadrature method (DQM) [32] was used. The DQM discretises the spatial variable so that the system of PDEs is transformed into a system of ordinary differential equations (ODEs) whose mass and stiffness matrices can be analysed using conventional numerical methods to obtain the modal properties (see Appendix C for more details). From the numerical studies, it was found that the DQM leads to the same results as the bvp4c for the beam-tendon with no pre-twist (shown in section 3.1) or for a pre-twisted beam with no tendon (shown in section 3.2). However, it was found that the DQM fails to converge for the beam-tendon with pre-twist and cannot therefore be used to obtain the modal parameters of the studied system on its own.

As a result of the numerical problems encounted by the DQM and the need for the starting guess when using bvp4c, these methods are used in the conjunction with each other to study the full beam-tendon system in section 4. Firstly, the DQM is used, but the pre-twist is set to zero. This provides a complete set of modal properties that are very close to the case when $\beta \neq 0$ and are therefore suitable as the starting guess for the bvp4c. The latter solver can then update the results for the pre-twisted beam. The final results in section 4 are therefore always obtained by the bvp4c solver and the DQM is merely used to provide a starting guess for all vibration modes.

The focus of the paper is on the effect of the applied force on the natural frequencies and the mode shapes of a rotating beam-tendon system. The natural frequencies will be presented mainly using two types of diagrams, namely frequency-loading diagrams which depict the evolution of the natural frequencies with the applied force, and Campbell diagrams which show the effect of the rotation (centrifugal forces) on the natural frequencies.

3. Validation of the developed model against literature

In this section, the numerical model developed is validated against results available in literature. Firstly, the comparison with [4] where a simplified beam-tendon system was experimentally validated is made, and then the Campbell diagram of a main rotor blade of a light helicopter is compared with the available reference to validate the under-lying beam model. This section is meant to not only validate the system of equations developed, but also show that both DQM and bvp4c give the same results for many cases.

3.1. Non-rotating beam-tendon model

The results obtained using the derived system of equations are compared to a simpler beam-tendon system studied experimentally in [4]. The main findings about the beam-tendon system are recapitulated in this section before diving into a more complicated case of the rotating pre-twisted beam with the cross-sectional coupling which was not studied in [4].

The beam-tendon system consists of a straight non-rotating beam with a rectangular cross-section that is loaded axially by a tendon. In [4], theoretical and experimental modal analysis of this system has been conducted and a number of frequency-loading diagrams have been measured. The system was also modelled using a simpler set of equations (no bending-torsional coupling, pre-twist and rotation were considered), theoretical modal analysis was carried out using the bvp4c solver and good correlation with the experimental data was obtained. The parameters of the system are $R = 1\,\mathrm{m}$, $EI_1 = 517.33\,\mathrm{N\,m^2}$, $EI_2 = 157.79\,\mathrm{N\,m^2}$, $GJ = 175.86\,\mathrm{N\,m^2}$, $m = 0.2929\,\mathrm{kg\,m^{-1}}$, $m_\mathrm{t} = 0.0125\,\mathrm{kg\,m^{-1}}$, $k_m = 0.0101\,\mathrm{m}$ and $e = e_A = \beta = \Omega = B_1 = B_2 = 0$.

The frequency-loading diagram of the beam-tendon system is shown in Fig. 2. It can be seen that there is no difference in the frequency loci computed by the DQM and bvp4c. The experimental results obtained in [4] are not included to maintain the focus on the main features of the beam-tendon system that can be summarised as follows

- There are two sets of modes - the frequency loci which appear to be almost parallel to the x-axis represent the beam-dominated modes while the frequency loci with the rapid increase in the frequency belong to the tendon. The natural frequencies of the beam-dominated modes slowly decrease with the increase in the applied load.

- Some of the modes veer [33] while some of them cross each other or pass through the veering region unaffected. This is given by the nature of the coupling as discussed in [4]. For example, in the red region highlighted in Fig. 2 two modes veer, and one passes through the veering region. The former two modes represent the beam bending and tendon transversal motions in the same direction. These two modes are coupled through the connection of the tendon and the beam at the tip, and hence they interact with each other. On the other hand, the latter frequency locus represents the tendon transversal motion in the orthogonal direction, which is not coupled to the former modes, and therefore does not feature veering. It can also be seen that the torsional mode does not veer with any of the tendon modes (see the blue highlight in Fig. 2) as it is not coupled to any of them.

- It can be seen in Fig. 2 that for low magnitudes of applied forces, there are many modes in the investigated frequency band. Many of these modes cannot be computed by the bvp4c because of its iterative nature which fails to converge even if an accurate starting guess is provided by the DQM. However, this is not considered to be a significant limitation, because the tendon-dominated modes for such a low applied force most likely have little to no significance in practice.

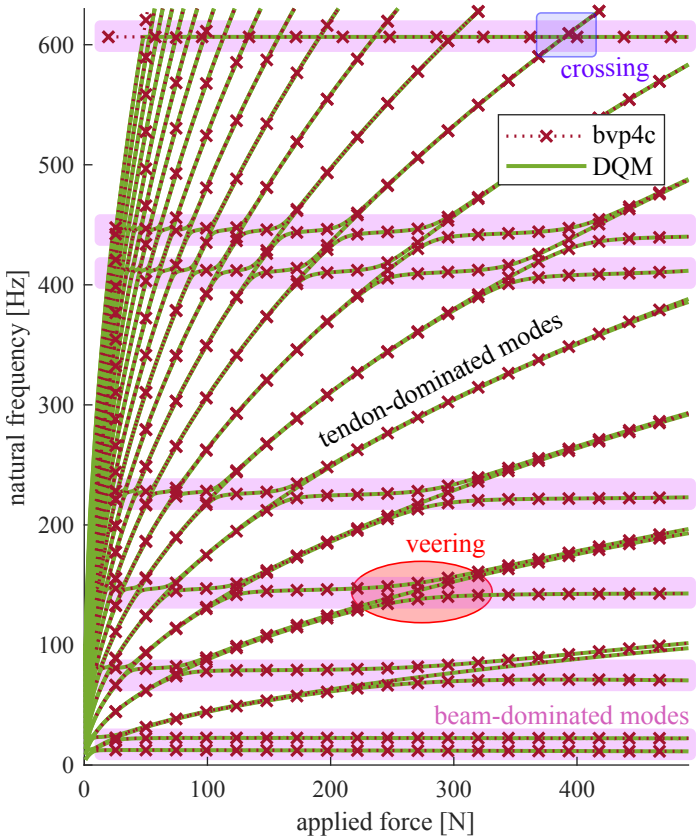

Figure 2: The frequency-loading diagram of the beam-tendon system studied in [4]. The two sets of modes can be observed - the beam-dominated modes whose natural frequencies are reduced by the applied load, and the tendon-dominated modes whose natural frequencies increase with the applied load. The two sets of modes interact with each other through frequency loci veering.

- In addition, the effect of the tendon mass was also established in [4], both numerically and experimentally. The natural frequencies of the tendon-dominated modes for heavier tendons are lower than those for lighter ones. This means that heavier tendons produce the frequency-loading diagrams that are more densely populated by the tendon-dominated modes than the same frequency-loading diagrams obtained for lighter tendons. Consequently, the veering regions shift so they appear at lower loading for lighter tendons. It was also found that the stability of the beam is not affected by the mass of the tendon, only by the applied axial force. It will be shown in section 4 that this is no longer true for a rotating system.

As can be seen from this summary, the beam-tendon system even without cross-sectional coupling, pre-twist and rotation exhibits rich dynamics. As the main focus of the paper is on a rotating, pre-twisted beam with cross-sectional coupling, a model of such a beam is validated against available literature in the next section.

3.2. Campbell diagram of a helicopter main rotor blade

A Bo105 helicopter is a a widely-used representative vehicle of a group of light, multi-purpose rotorcraft deployed for medical services, police, search and rescue, and military missions. A blade of its four-bladed hingeless main rotor is investigated here, also because this helicopter is used as a reference aircraft in the SABRE project [1]. The purpose of this section is to introduce the under-lying blade model before including the tendon in the system. Since the non-uniform structural parameters of the blade are not publicly available, the uniform parameters, which lead to equivanlent results in terms of the Campbell diagrams, are used

instead. These are $R = 4.912\,\mathrm{m}$, $EI_1 = 10\,000\,\mathrm{N\,m^2}$, $EI_2 = 170\,000\,\mathrm{N\,m^2}$, $GJ = 4850\,\mathrm{N\,m^2}$, $m = 5.5\,\mathrm{kg\,m^{-1}}$, $k_{m1} = 0.009\,\mathrm{m}$, $k_{m2} = 0.0648\,\mathrm{m}$, $e = -0.01\,\mathrm{m}$, $e_A = 0\,\mathrm{m}$, $k_A = 0.041\,\mathrm{m}$ and $B_1 = B_2 = 0$. An equivalent initial linear pre-twist characterised by $\beta(x) = -0.022x + 0.0663\,\mathrm{rad}$ is also considered, and the rotorcraft operates with the nominal rotor speed of $\Omega_{\mathrm{nom}} = 44.4\,\mathrm{rad\,s^{-1}}$.

The computed Campbell diagram and selected mode shapes can be seen in Fig. 3. The first ten computed

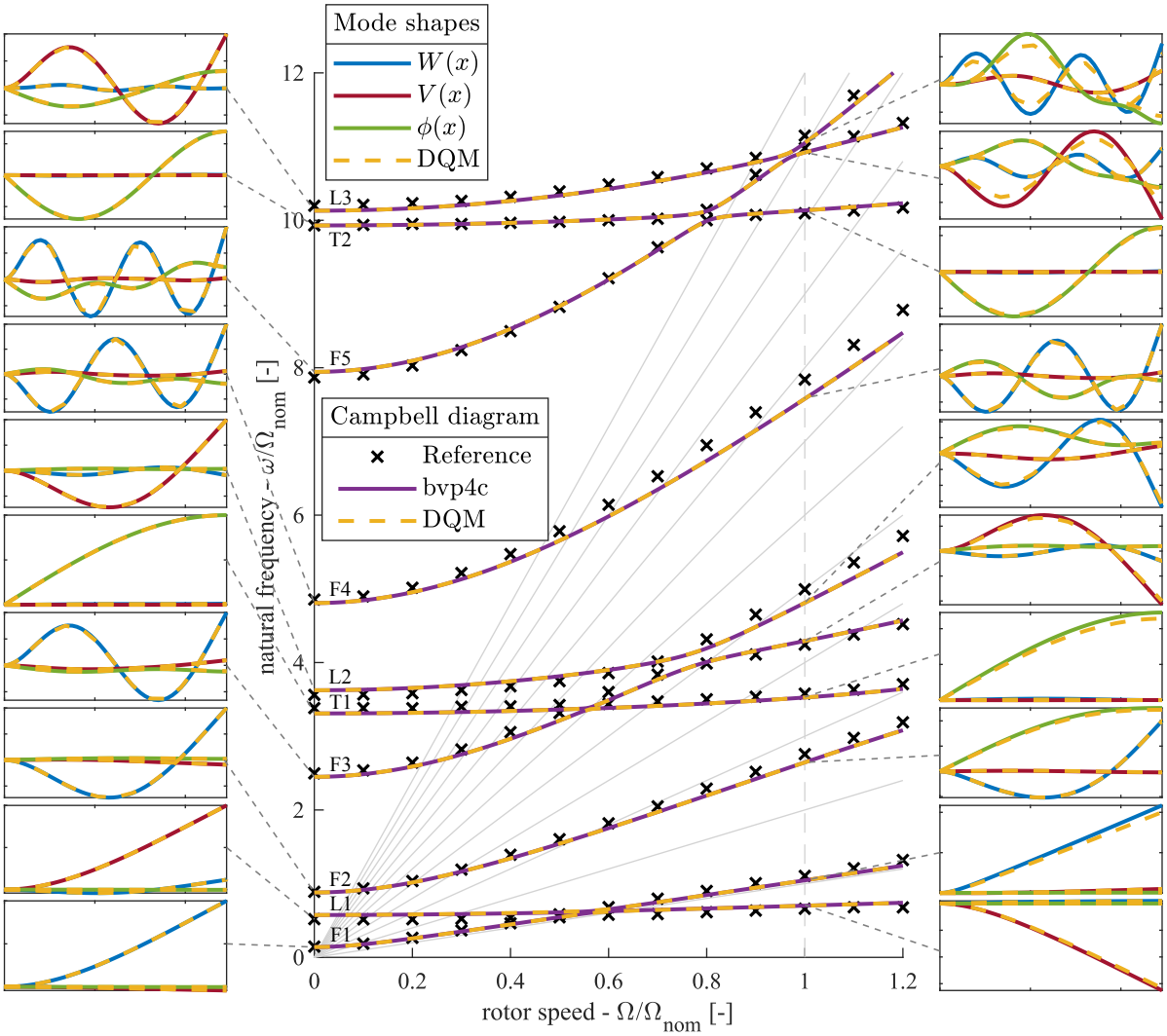

Figure 3: The Campbell diagram of a beam with uniform parameters and linear pre-twist representing a main rotor blade of a light rotorcraft. The label Fx marks the x-th flapping-dominated mode, Lx stands for the x-th lead-lad-dominated mode, and Tx for the x-th torsion-dominated mode. The insets on the left and right side of the Cambell diagram show the coupled mode shapes (the x-axis represents the span of the blade x and the y-axis is the normalised value of the mode shape)

frequencies are compared to the reference which was computed using a finite element code for non-uniform parameters and validated against measurements [1]. Overall, the match between the computed results and the reference is satisfactory, although there are small differences between them caused by the use of the equivalent parameters.

The frequency of each mode increases due to the stiffening effect of the centrifugal forces. The rate of increase is different for each mode, with the torsion-dominated modes (marked by T1 and T2) featuring almost no increase, and the bending-dominated modes increasing more rapidly. Since all the motions are coupled, all the modes veer with each other.

From the shown mode shapes, it is clear that all three motions are coupled and, especially for higher modes, it is no longer possible to characterise them as pure flapping, lead-lag or torsional modes. In addition, the swap of the mode shapes due to veering can be observed. For example, the first two modes for the non-rotating case ($\Omega = 0$) changed the mode shape at the nominal rotor speed due the veering. It should be noted that in the frequency-loading diagram in Fig. 2 the veering is caused by the tendon-induced axial loading, while in the Campbell diagram in Fig. 3 it is caused by the centrifugal effects. In the full model of the rotating beam-tendon system these two effects are combined and therefore lead to more complex behaviour.

It can be seen that the DQM led to the same results as the bvp4c, even when the pre-twist is present. However, this could only be achieved by selecting a very fine discretisation, and could not be done at all when the tendon was present in the system. In that case, the DQM would not converge to correct results. Therefore, the combination of the DQM and bvp4c as described in section 2 is used in the rest of the paper.

4. Free vibration analysis of a pre-twisted rotating beam loaded by a tendon

Having validated the numerical procedure for the non-rotating beam-tendon system, and the rotating pre-twisted beam, a rotating beam-tendon system is investigated in this section. Firstly, a range of allowed loading is studied, then the frequency-loading and Campbell diagrams are discussed. The obtained results are related to the findings made for the non-rotating and uncoupled case summarised in section 3.1 with emphasis on the effect of the rotation and coupling. Throughout the section, the parameters of the beam from section 3.2 are used and the numerical procedure described in section 2.2 is employed. Three different tendon masses are investigated, with m_t equal to 1 %, 5 % or 10 % for the beam mass m.

4.1. Structural stability of the beam-tendon system

As the beam is axially loaded the structural stability determines the maximum allowed loading. The loss of structural stability occurs at the critical force P_cr when the lowest natural frequency of the system drops to zero [27, 28, 34]. The computed critical force P_cr can be seen in Fig. 4 for all three tendon masses. The

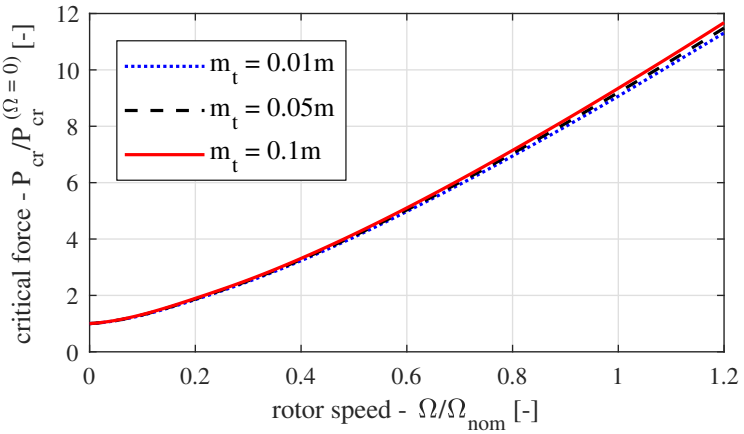

Figure 4: The critical forces computed for different rotor speeds and tendon masses, and normalised by the critical force for the non-rotating beam $P_\mathrm{cr}^{(\Omega=0)}$.

critical force is a function of the rotor speed due to the stiffening effect of the centrifugal force and divides the investigated loading region into two parts:

- $P < P_\mathrm{cr}$ - *tendon working region* - the applied force is lower than the critical force and therefore, this is the region of interest which will be investigated further.

- $P_{\mathrm{cr}} < P$ - *structural instability* - the system does not vibrate as the beam diverges due to the applied axial load. This loading region is not further investigated in this paper.

It can be also seen in Fig. 4 that the critical force depends on the mass of the tendon. It would seem that the critical force should not depend on the mass of the tendon since the loss of stability occurs due to the divergence of the beam subjected to the axial loading. However, the stability is determined not only by the amount of the axial force, but also by the involved boundary conditions. In particular, Eqs. (3a) and (3c) give the shear forces at the end of the beam, where the terms Pw_{t}' and Pv_{t}' determine the contribution of the tendon. For the non-rotating case, the critical force is the same for any tendon mass because both axial force and the slope of the tendon are the same for any tendon. This is true because the mode shapes of a taut string with uniformly distributed tension do not depend on its mass, as known from analytical solutions [6]. However, when the system rotates, the centrifugal force causes non-uniform distribution of the tendon tension. Because the centrifugal force depends on the mass, the tendon tension depends on the mass as well and so does its mode shape. Consequently, the slopes of the tendon at the tip (w_{t}' and v_{t}') depend on the mass of the tendon and so does the critical force. It can be seen that the critical force at the nominal rotor speed is approximately nine times higher than at rest for any tendon mass.

4.2. Frequency-loading diagram of the first two beam-dominated modes

It is known from classical stability studies [27, 28] that the decrease of the lowest natural frequency of a cantilever beam caused by an axial force is not linear. In order to examine the evolution of the first two frequency loci (F1 and L1 modes) for non-rotating and rotating beam, they are shown in Fig. 5. In

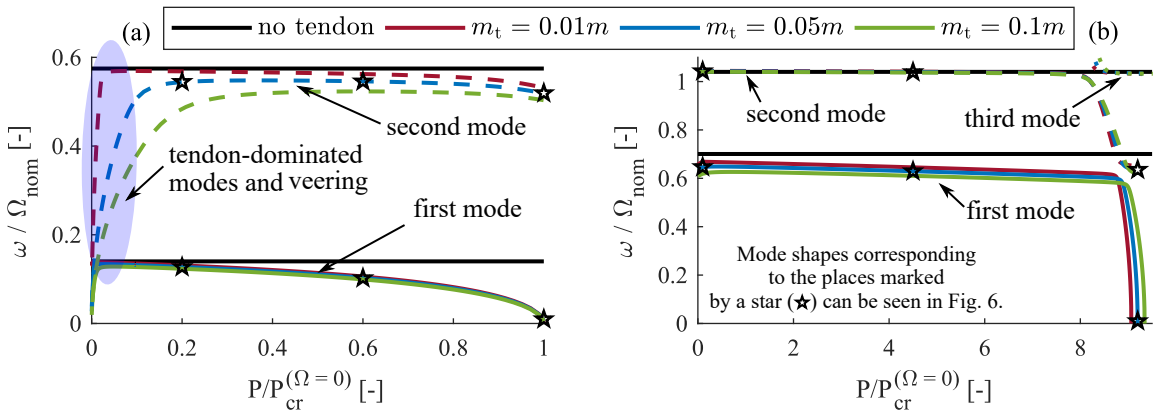

Figure 5: Reduction of the first two natural frequencies for 0.01m, 0.05m and 0.1m for (a) $\Omega = 0$ (b) $\Omega = \Omega_{nom}$. The x-axis shows the applied loads normalised by the critical force for the non-rotating beam $P_{\mathrm{cr}}^{(\Omega=0)}$, and the y-axis represents the natural frequencies normalised by the nominal rotor speed Ω_{nom}.

Fig. 5(a) it can be seen that the critical force of the non-rotating beam-tendon system does not depend on the mass of the tendon. The frequency loci for the beam-tendon system are close to the beam's nominal frequencies (black horizontal lines) for low loading. With increasing loading, the frequency loci of the first two modes decrease. The decrease is initially gradual, almost linear, but rapid close to the critical force. At the very low applied force (marked by the purple ellipse in Fig. 5(a)), it can be seen the frequency loci of both modes seemingly decrease towards zero. However, at this region, the shown frequency loci belong to the first tendon-dominated mode which veer with the first two beam-dominated modes.

In Fig. 5(b) the frequency loci of the rotating system ($\Omega = \Omega_{\mathrm{nom}}$) are shown. It can be seen that the frequency loci are qualitatively different to the non-rotating case. The critical force is significantly higher and depends on the tendon mass (as already seen in Fig. 4). There is no veering at the very low applied force because the natural frequency of the first tendon-dominated modes is higher due to the centrifugal force acting on the tendon. However, it can be seen that the first, second and also third frequency loci veer

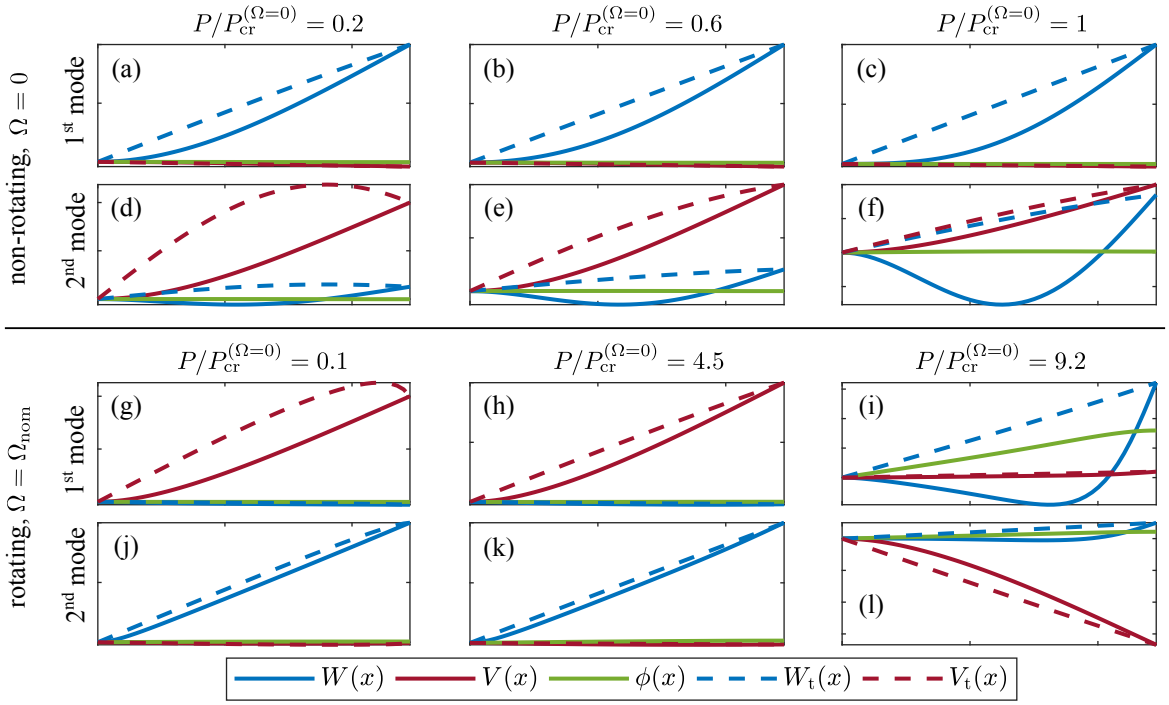

Figure 6: The first two mode shapes of the rotating and non-rotating beam-tendon system with $m_{\mathrm{t}} = 0.05m$. The corresponding natural frequencies can be seen in Fig. 5.

with each other close to the critical force. This veering is caused by the coupling between the flapping and lead-lag motion which is given by the pre-twist.

The mode shapes corresponding to natural frequencies marked by black stars in Fig. 5 can be seen in Fig. 6. It can be seen in the first row in Fig. 6 that the first mode of the non-rotating system is associated with pure flapping motion. The typical shape of the first bending mode can be observed and the tendon is spanned between the root and the tip of the beam in a straight line. On the other hand, more complicated mode shapes can be seen in the second row in Fig. 6 which represent the second mode of the non-rotating beam-tendon system. Although the second mode should be dominated by the first lead-lag bending mode, there is a mix of the first lead-lag and second flap-wise bending. Moreover, the mix becomes more apparent with the increased applied load and the contribution of the two modes is practically equal in Fig. 6(f). This mixture of the mode shapes is caused by the veering between the first lead-lag and second flapping modes. These two modes approach each other because the reduction of the F2 natural frequency is more significant than the reduction of L1 mode. This will be later seen in Fig. 7(a) as well.

The third row in Fig. 6 shows the first mode of the rotating beam-tendon system. It can be seen in Fig. 6(g) that for very low applied force, the first lead-lag mode is observed, but the tendon is not a straight line spanned from the tip to the clamp. The tendon therefore does not reach the maximum deflection at the tip, but rather close to it. This is caused by the centrifugal force that dominates the internal tension. In Fig. 6(h) the tendon is already spanned in the straight line between the tip and the clamp due to the applied force. In this case, the centrifugal force is still present, but it is much lower than the applied force so the peak deflection close to the tip is not manifested. In Fig. 6(i) the first lead-lag mode is replaced by the second flapping mode. This is possible due to the strong veering of the second flapping mode whose frequency locus is rapidly decreasing with the applied force as will be seen in Fig. 7(b). In addition, torsion can be also observed in this mode due to the cross-sectional coupling. Therefore, the shape of the blade divergence at rotation is given by the second flapping mode coupled with torsion as opposed to the pure first flapping mode when at rest. This is an important qualitative feature which should be taken into account if the structural stability is investigated further.

In the fourth row in Fig. 6 the second mode of the rotating blade-tendon system can be seen. The first two subplots (Fig. 6(j) and Fig. 6(k)) show the first flapping mode. At rest, the second mode was dominated by the lead-lag motion, but at rotation it changed due to the centrifugal stiffening. In Fig. 6(l) a mixture of the first lead-lag and second flapping mode can be seen. This is again caused by the veering better seen in Fig. 7(b).

In this section, the operating region of the beam-tendon system has been established and it has been shown how the first two frequency loci change with the applied load. The numerical results were obtained for three tendon masses and it can be concluded that the mass of the tendon has an effect on the frequency reduction and the critical force. However, the tendon mass does not affect the qualitative behaviour of the beam-tendon system significantly. Therefore, the rest of the analysis in this paper will be carried out for the middle tendon mass case, with $m_t = 0.05m$.

4.3. Full frequency-loading diagram

The frequency-loading (F-L) diagrams of the non-rotating and rotating beam-tendon system can be seen in Fig. 7. The position of the natural frequencies of the beam (without tendon) are also indicated. These

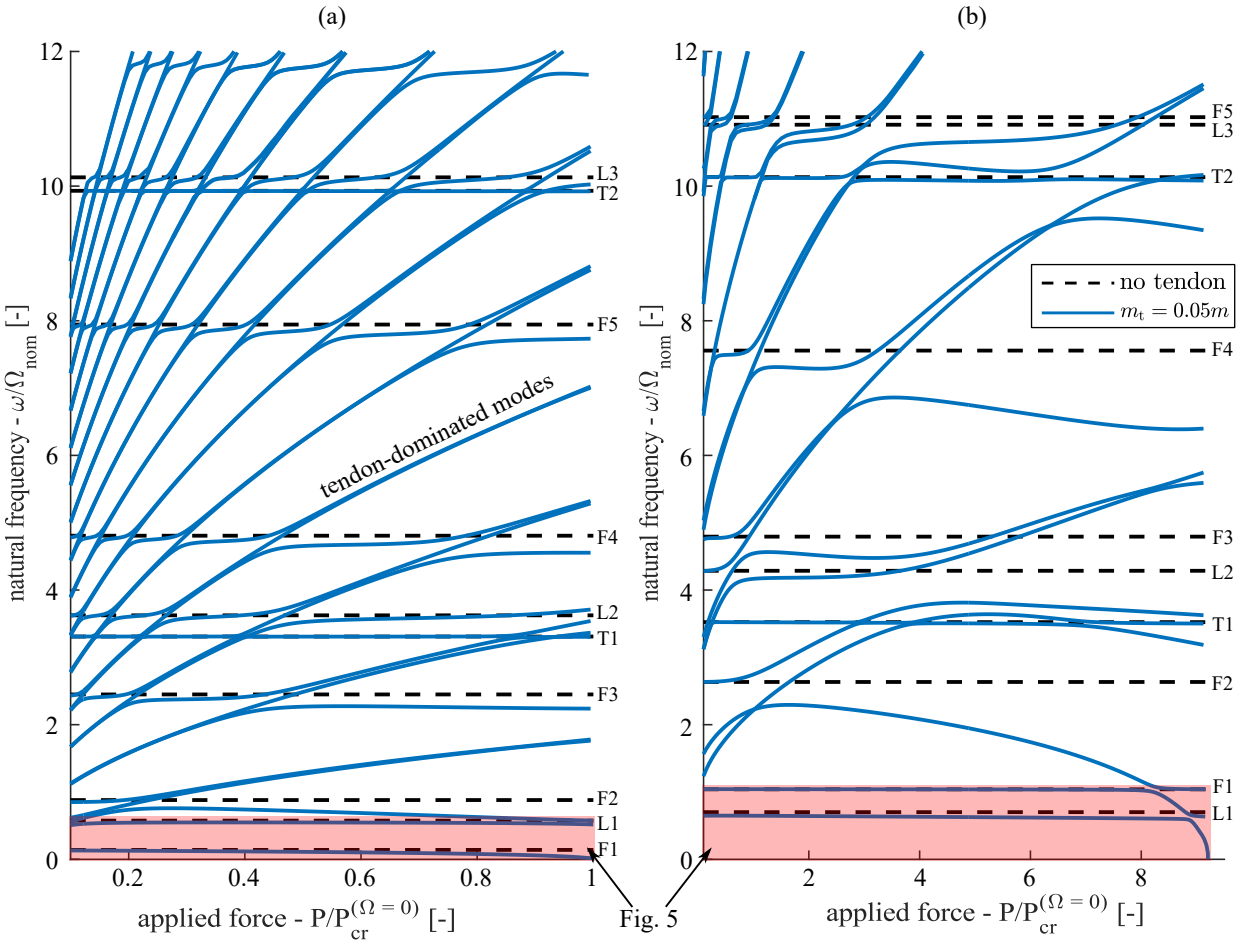

Figure 7: Frequency-loading diagram for $m_t = 0.05m$ for (a) $\Omega = 0$ and (b) $\Omega = \Omega_{nom}$. For the rotating case, the frequency reduction of the beam-dominated modes is more significant and the veering regions are wider.

F-L diagrams are extensions of Fig. 5 for the first ten modes. It can be seen that the character of the F-L diagrams for rotating and non-rotating system is significantly different. Both of them contain beam-dominated and tendon-dominated modes that veer with each other. However, all the veering regions in the

rotating systems are much wider. This is arguably because of the fact that the centrifugal force and axial loading are applied at the same time.

The frequencies of all beam-dominated modes are reduced by the tendon-induced axial loading. The amount of the frequency reduction vary for individual modes, and rotating and non-rotating case. The frequencies of the torsional modes decrease only very little, but unlike in Fig. 2 the torsional modes veer with all other tendon-dominated and beam-dominated modes. Such veering will be described in detail in section 4.4.

The reduction in the natural frequencies was identified as the mechanism that allows an application of an active tendon concept in rotorcraft for the resonance avoidance [2]. The reduction therein was achieved solely by the axial force and the tendon was not explicitly modelled. Although the present results show that the reduction can be achieved when the tendon is included, a large number and variety of veering regions is also seen. This makes the F-L diagram of the rotating system look complex and may lead to a conclusion that the presence of the tendon could limit the resonance avoidance effect as there are many tendon-related resonances that can be excited. However, it is important to note that the tendon-dominated modes can be easily damped. In addition, the mass of the tendon is significantly lower than the mass of the beam and therefore they are not necessarily energetically significant. Moreover, it might be possible to utilise the veering as an active vibration absorber. This possibility is briefly investigated in [35], but it requires further research.

4.4. Campbell diagram

In this section, the Campbell diagram from Fig. 3 is recomputed for the blade-tendon system. The applied load is equal to the 50 % of the critical force P_{cr} at each rotor speed. The applied force therefore depends on the rotor speed in a similar manner as in Fig. 4.

The Campbell diagram of the beam-tendon system can be seen in Fig. 8. For the low frequency, there are many tendon-dominated modes. They always appear in pairs - one frequency locus for each transversal direction. However, once they start veering with the beam-dominated modes, their trajectories split. The tendon-dominated frequency loci increase rapidly with the applied force which means that many of them leave the investigated frequency region before the nominal rotor speed is reached.

The mode shapes shown on the left and right side represent the beam-dominated modes (the same ones as in Fig. 3). However, the tendon mode shape components are also included. It can be seen that the tendon and the beam have always the same displacement at the tip as per the boundary conditions. The beam-dominated mode shapes are similar to those shown in Fig. 3. However, some influence of the tendon can still be seen. This is particularly visible at the nominal rotor speed for the third mode when compared to the corresponding mode shape from Fig. 3. It can also be seen that for the non-rotating system the higher tendon modes with many nodes of vibration are present. However, due to veering and rapid increase in their frequency loci with the applied force, these higher modes leave the frequency region of interest. For example, the tenth mode of the beam (L3) is combined with the 8^{th} mode of the tendon at rest, but only with the 3^{rd} tendon mode at the nominal rotor speed.

There is no crossing in the Campbell diagram as all the frequency loci veer with each other. In order to further explore the coupling between the tendon and the torsional modes, which are not directly coupled in the PDEs or BCs, a section of the Campbell diagram is enlarged in Fig. 9. From the displayed mode shapes, it can be seen that all of them changed their places. For example, the first mode from the bottom on the left becomes the last mode on the right while it veered several times in between. In the small inset, it can be seen that the veering even occurs at very small scale with the smallest distance between the frequency loci being less than $0.002\ \Omega/\Omega_{\mathrm{nom}}$. This narrow veering modal interaction is observed between the torsional mode and the mode that is dominated by the motion of the tendon in the lead-lag direction. These two motions are not directly coupled in the PDEs or BCs. However, they are indirectly coupled where the torsion is coupled to the flapping via the offset of the elastic and mass axis, flapping is coupled to the lead-lag through the pre-twist, and the tendon is coupled with the flapping and lead-lag through its attachment to the tip of the beam. It is believed that this indirect coupling is responsible for the small veering region.

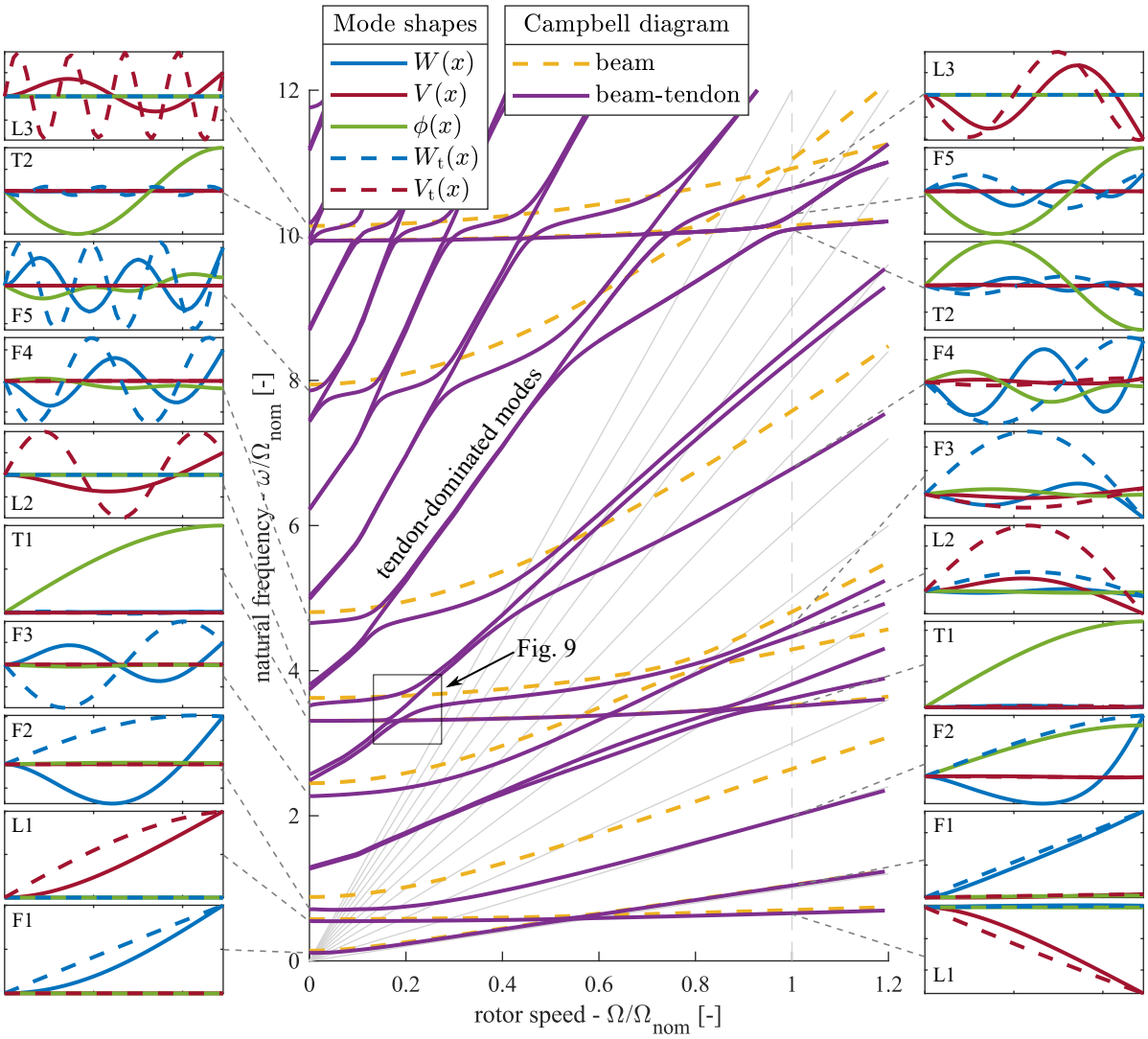

Figure 8: The frequency diagram the beam-tendon system for $m_t = 0.05m$ and $P = 0.5P_{\mathrm{cr}}(\Omega)$ and the selected mode shapes. The same type of mode shapes as in Fig. 3 were selected so the influence of the tendon can be observed.

5. Discussion

In this paper, the theoretical model of the beam-tendon system was derived by the principle of the minimum potential energy. It was assumed that the rotating, pre-twisted beam meets all the assumptions of the Euler-Bernoulli theory. Therefore, the model does not take into account the transverse shear deformation, rotary inertia effects, warping and material diversity of a typical rotorcraft blade. This may certainly be seen as a limitation with regards to rotorcraft blade modelling, which is usually made of composites may be more accurately modelled using more sophisticated approaches such as geometrically-exact, fully intrinsic composite blade theory [8] or three-dimensional linear elasticity-based model [36, 37]. However, it is believed that the main findings made for the beam-tendon system presented in this paper, such as the frequency reduction and frequency loci veering, would be also present if a different beam model was used. While the frequency reduction and frequency loci veering should still be observed regardless of the used beam model, the amount of frequency reduction and the location of veering regions may differ depending on the used beam model. Therefore, the future studies should investigate how different beam models influence the

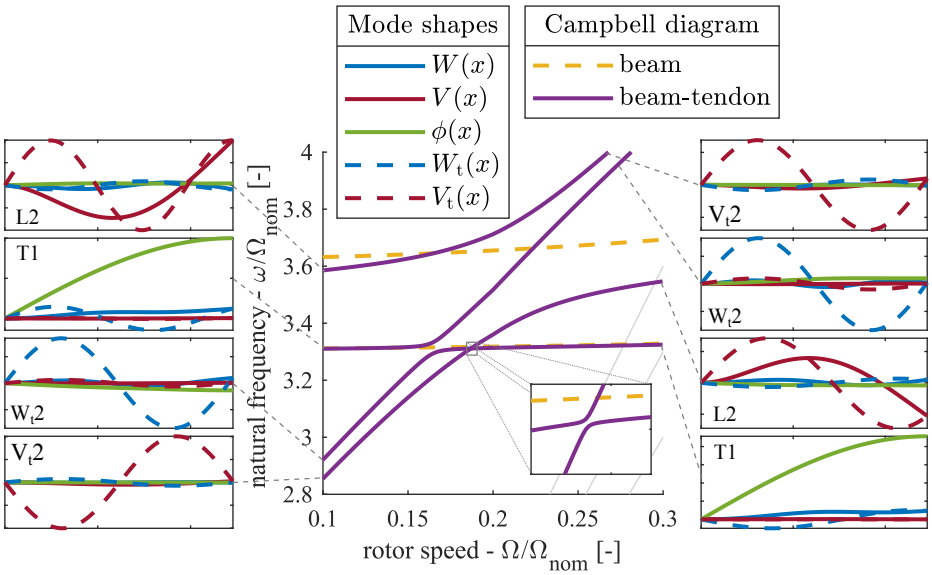

Figure 9: Detail of the veering region from Fig. 8. The torsional modes in 3rd and 1st inset on the left and right side of the graph, respectively, are multiplied by 0.1 to decrease their amplitude in order to see their coupling with other mode shape components.

dynamics of a beam-tendon system. Moreover, in practice the beam model that is most suitable for a given application should be used and its suitability and accuracy should be experimentally validated.

Since the developed model is a system of coupled PDEs and BCs, it cannot be solved analytically and the numerical analysis must be therefore employed. It was proposed to use a combination of the bvp4c [31] and DQM [32] solvers to obtain the final results. This was needed because the DQM would not converge to the correct results for the pre-twisted beam-tendon system, but would be able to provide a very good starting guess for the subsequent bvp4c computations. Although the employed procedure works well, it is acknowledged that further method improvements may be needed to evaluate results in the regions with many tendon-dominated modes. An entirely different solution procedure could also be tried in the future. The numerical implementation was validated against the results of the non-rotating, uncoupled beam-tendon system without pre-twist, and the rotating, pre-twisted beam model. The former validation case introduced the features of the beam-tendon system, where it was shown that only some of the modes veer, while other cross, depending on the coupling between them.

In section 4, the rotating, pre-twisted beam-tendon system was investigated. The results were evaluated with reference to the previously validated case for a non-rotating beam-tendon system. It was found that all the modes exhibit veering due the the coupling of both bending directions and torsion of the beam due to the presence of the offset between the elastic and mass axes, and the blade pre-twist. Additionally, it was observed that the veering regions were significantly wider when the system rotated. It is believed that a combination of the rotating and axial loading is responsible for this phenomenon.

The structural stability was also investigated in section 4.1. The critical force was determined by the divergence of the beam which, in this case, depends on the rotor speed and mass of the tendon. It was shown that the mode shape associated with the loss of stability is different for the rotating and non-rotating system. The former is the first flap-wise bending mode, whereas the latter is the second flapping mode coupled with torsion.

The present paper was motivated by the future application of an active tendon concept in rotorcraft as investigated within the SABRE project [1, 3]. It was already shown [2, 38] that the axial force alone has potential to allow rotorcraft to operate with variable rotor speed. This paper indicates that the tendon can be used to induce this axial force which consequently reduces the natural frequencies of the blade. However, it was also observed that many tendon-dominated modes, and therefore potential resonances, emerge in

the Campbell diagram. Although this may seem as a potential problem, it is assumed that the tendon can be easy damped, attached in a several spanwise locations [30] or guided thought the blade. It is also possible that the tendon's resonances will have little effect on the blade given the difference in their masses. Moreover, it is believed that the veering, caused by the interaction between the tendon-dominated and beam-dominated modes, can be utilised as a vibration absorber, and hence further enhance the capabilities of an active tendon concept. A preliminary investigation of this possibility has been already conducted in [35], but a more systematic investigation is needed.

6. Conclusions

In this paper, a rotating, pre-twisted beam loaded by a tendon-induced axial force has been investigated for the first time. The theoretical model of the system was derived using the principle of minimum potential energy, the numerical free vibration analysis conducted using a combination of a boundary value problem solver and the differential quadrature method, and the computed frequency-loading and Campbell diagrams evaluated. The focus was on the effect of rotation, pre-twist and cross-sectional coupling on the modal characteristics of the beam-tendon system. From the numerical studies conducted, it can be concluded that the rotating beam-tendon system exhibits the same features as its non-rotating counterpart, i.e. the frequency reduction and frequency loci veering. However, these features are significantly affected by the rotation and cross-sectional coupling. In particular, it was shown that the presence of the offset between the mass and elastic axes and the beam's pre-twist causes the coupling between all beam-dominated and tendon-dominated modes, leading to a complex appearance of the frequency-loading and Campbell diagrams due to a number of veering regions. In addition, it was demonstrated that when the system rotates the veering regions are wider and the critical force, which leads to the loss of stability, is considerably higher. The paper finishes with remarks about the application of the beam-tendon system in rotorcraft for resonance avoidance. It is concluded that the beam-tendon system can be utilised for this application not only because of the frequency reduction due to the tendon-induced axial force, but also because of the frequency loci veering.

Acknowledgements

The authors would like to acknowledge the financial support of the European Community's Horizon 2020 Program provided through the project "Shape Adaptive Blades for Rotorcraft Efficiency (SABRE)", Grant Agreement 723491.

References

[1] J. Rauleder, B. G. van der Wall, A. Abdelmoula, D. Komp, S. Kumar, V. Ondra, B. Titurus, B. K. S. Woods, Aerodynamic Performance of Morphing Blades and Rotor Systems, in: AHS International 74th Annual Forum & Technology Display, Phoenix, Arizona, USA, 2018.
[2] R. Dibble, V. Ondra, B. Titurus, Resonance avoidance for variable speed rotor blades using an applied compressive load, Aerospace Science and Technology 88 (2019) 222 – 232. doi:10.1016/j.ast.2019.03.009.
[3] V. Ondra, R. Dibble, B. Titurus, Towards an application of an active tendon in rotorcraft: A numerical and experimental study of coupled bending-torsion vibration of a beam-tendon system, in: International Conference on Noise and Vibration Engineering (ISMA2018), 2018.
[4] V. Ondra, B. Titurus, Theoretical and experimental modal analysis for a beam-tendon system, Mechanical systems and signal processing 132 (2018) 55–71. doi:10.1016/j.ymssp.2019.06.016.
[5] R. Dibble, B. Titurus, Helicopter rotor blade modal tuning using internal preloads, in: International Conference on Noise and Vibration Engineering (ISMA2016), 2016.
[6] S. S. Rao, Vibration of Continuous Systems, 2007.
[7] A. Rosen, Structural and dynamic behaviour of pretwisted rods and beams, Applied Mechanics Reviews 44 (12) (1991) 483–515.
[8] D. Hodges, Nonlinear Composite Beam Theory, American Institute of Aeronautics and Astronautics, 2006.
[9] M. Rafiee, F. Nitzsche, M. Labrosse, Dynamics, vibration and control of rotating composite beams and blades: A critical review, Thin-Walled Structures 119 (January) (2017) 795–819. doi:10.1016/j.tws.2017.06.018.

[10] Sinha, Sunil K. and Turner, Kevin E., Natural frequencies of a pre-twisted blade in a centrifugal force field, Journal of Sound and Vibration 330 (11) (2011) 2655 – 2681. doi:10.1016/j.jsv.2010.12.017.
[11] Chakshu, Neeraj Kavan and Sinha, Sunil K., Natural Frequencies of Pre-Twisted Airfoil Blades, in: ASME 2017 Gas Turbine India Conference, 2017, p. V002T05A019. doi:10.1115/GTINDIA2017-4722.
[12] Gu, X.J. and Hao, Y.X. and Zhang, W. and Liu, L.T. and Chen, J., Free vibration of rotating cantilever pre-twisted panel with initial exponential function type geometric imperfection, Applied Mathematical Modelling 68 (2019) 327 – 352. doi:10.1016/j.apm.2018.11.037.
[13] G. Isakson, J. G. Eisley, Natural frequencies in coupled bending and torsion of twisted rotating and nonrotating blades (1964).
[14] S.-M. Lin, J.-F. Lee, S.-Y. Lee, W.-R. Wang, Prediction of vibration of rotating damped beams with arbitrary pretwist, International Journal of Mechanical Sciences 48 (12) (2006) 1494–1504. doi:10.1016/j.ijmecsci.2006.05.015.
[15] J. C. Houbolt, G. W. Brooks, Differential equations of motion for combined flapwise bending, chordwise bending, and torsion of twisted nonuniform rotor blades (1957).
[16] D. H. Hodges, E. H. Dowell, Nonlinear equations of motion for the elastic bending and torsion of twisted nonuniform rotor blades (1974).
[17] S.-Y. Lee, S.-M. Lin, Y.-S. Lin, Instability and vibration of a rotating timoshenko beam with precone, International Journal of Mechanical Sciences 51 (2) (2009) 114 – 121. doi:10.1016/j.ijmecsci.2008.12.008.
[18] Sinha, Sunil K., Non-linear dynamic response of a rotating radial timoshenko beam with periodic pulse loading at the free-end, International Journal of Non-Linear Mechanics 40 (1) (2005) 113 – 149. doi:10.1016/j.ijnonlinmec.2004.05.019.
[19] Sinha, Sunil K., Combined torsional-bending-axial dynamics of a twisted rotating cantilever timoshenko beam with contact-impact loads at the free end, Journal of Applied Mechanics 74 (2) (2006) 505 – 522. doi:10.1115/1.2423035.
[20] A. H. Nayfeh, P. F. Pai, Linear and Nonlinear Structural Mechanics, Wiley, 2008.
[21] S. Korkmaz, A review of active structural control: challenges for engineering informatics, Computers and Structures 89 (23-24) (2011) 2113–2132. doi:10.1016/j.compstruc.2011.07.010.
[22] A. Preumont, Vibration Control of Active Structures: An Introduction, Springer Netherlands, 2012.
[23] S. Lenci, F. Clementi, C. Mazzilli, Simple formulas for the natural frequencies of non-uniform cables and beams, International Journal of Mechanical Sciences 77 (2013) 155 – 163. doi:10.1016/j.ijmecsci.2013.09.028.
[24] S. Nudehi, R. Mukherjee, S. Shaw, Active vibration control of a flexible beam using a buckling-type end force, Journal of Dynamic Systems, Measurement, and Control 128 (2) (2006) 278. doi:10.1115/1.2192836.
[25] J. Issa, R. Mukherjee, S. Shaw, Vibration suppression in structures using cable actuators, Journal of Vibration and Acoustics 132 (3) (2010) 031006. doi:10.1115/1.4000783.
[26] P. Thomson, G. Balas, P. Leo, The use of shape memory alloys for passive structural damping, Smart Materials and Structures 4 (1) (1995) 36.
[27] L. Virgin, Vibration of Axially-Loaded Structures, Cambridge University Press, 2007.
[28] Z. Bazant, L. Cedolin, Stability of Structures: Elastic, Inelastic, Fracture and Damage Theories, World Scientific, 2010.
[29] G. Cheng, J. W. Zu, Dynamic analysis of an optical fiber coupler in telecommunications, Journal of Sound and Vibration 268 (1) (2003) 15–31. doi:10.1016/S0022-460X(02)01575-4.
[30] V. Ondra, B. Titurus, Numerical and experimental modal analysis of a cantilever beam axially loaded by a tendon which is attached in a single spanwise location, in: M. L. Mains, B. J. Dilworth (Eds.), Topics in Modal Analysis & Testing, Volume 8, Springer International Publishing, Cham, 2020, pp. 107–116. doi:10.1007/978-3-030-12684-1_10.
[31] J. Kierzenka, L. Shampine, A BVP solver based on residual control and the Matlab PSE, ACM Transactions on Mathematical Software 27 (3) (2001) 299–316. doi:10.1145/502800.502801.
[32] C. Bert, M. Malik, Differential quadrature method in computational mechanics: A review, Applied Mechanics Reviews 49 (1) (1996) 1–28. doi:10.1115/1.3101882.
[33] B. R. Mace, E. Manconi, Wave motion and dispersion phenomena: Veering, locking and strong coupling effects, The Journal of the Acoustical Society of America 131 (2) (2012) 1015–1028. doi:10.1121/1.3672647.
[34] S. Timoshenko, J. Gere, Theory of Elastic Stability, Engineering societies monographs, Dover Publications, 1961.
[35] V. Ondra, R. Dibble, B. K. S. Woods, B. Titurus, An active tendon concept in rotorcraft with variable speed rotors: free vibration perspective, in: AIAA Scitech 2019 Forum, 2019. doi:10.2514/6.2019-0857.
[36] Filiz, Sinan and Bediz, Bekir and Romero, L.A. and Ozdoganlar, O. Burak, Three dimensional dynamics of pretwisted beams: A spectral-tchebychev solution, Journal of Sound and Vibration 333 (10) (2014) 2823 – 2839. doi:10.1016/j.jsv.2014.01.010.
[37] Bediz, Bekir and Romero, L.A. and Ozdoganlar, O. Burak, Three dimensional dynamics of rotating structures under mixed boundary conditions, Journal of Sound and Vibration 358 (2015) 176 – 191. doi:10.1016/j.jsv.2015.08.015.
[38] R. Dibble, V. Ondra, B. K. S. Woods, B. Titurus, Aeroelastic eigenvalue analysis of a variable speed rotor blade with an applied compressive load, in: AIAA Scitech 2019 Forum, 2019. doi:10.2514/6.2019-1355.
[39] L. F. Shampine, J. Kierzenka, W. Reichelt, Mark, Solving Boundary Value Problems for Ordinary Differential Equations in Matlab with bvpc.

Appendix A. Derivation of the equations of motion and boundary conditions

The equations of motion and the corresponding boundary conditions given in section 2.1 can be derived using the principle of minimum potential energy

$$\delta\Pi = \delta U - \delta W = 0, \tag{A.1}$$

where U is the strain energy and W is the potential energy of the applied loads [6]. The total potential energy U of the system is given by [15]

$$U = \frac{1}{2}\int_0^R \Big\{ EI_1(v''\sin\beta - w''\cos\beta)^2 + EI_2(v''\cos\beta + w''\sin\beta)^2 + \\ \left[GJ + EB_1(\beta')^2\right]\phi'^2 - 2EB_2(v''\cos\beta + w''\sin\beta)\beta'\phi' \underline{+P(w_t'^2 + v_t'^2)} \Big\}\,\mathrm{d}x, \tag{A.2}$$

where the underlined terms account for the presence of the tendon in the system and the notation is the same as in the main body of the paper. The work W is given by [15]

$$W = \int_0^R \Bigg(\overline{T}\Big\{ -\frac{1}{2}\left[v'^2 + w'^2\right] + e_A(v''\cos\beta + w''\sin\beta) - e_A\phi(v''\sin\beta - w''\cos\beta) - k_A^2\left[\frac{1}{2}\phi'^2 + \beta'\phi'\right]\Big\} + \\ \Omega^2 m\Big\{ xe\left[-(v'\cos\beta + w'\sin\beta) + \phi(v'\sin\beta - w'\cos\beta)\right] + \frac{1}{2}v^2 + (e\cos\beta + e_0 - e\phi\sin\beta)v + \\ \Big[-\left(k_{m2}^2 - k_{m1}^2\right)\sin\beta\cos\beta - ee_0\sin\beta\Big]\phi - \frac{1}{2}\Big[\left(k_{m2}^2 - k_{m1}^2\right)\cos 2\beta + ee_0\cos\beta\Big]\phi^2\Big\} \\ + p_y v + p_z w + q\phi \underline{+\frac{1}{2}T_t[v_t'^2 + w_t'^2] + \frac{1}{2}\Omega^2 m_t v_t^2 + p_{v_t}v_t + p_{w_t}w_t} \Bigg)\,\mathrm{d}x, \tag{A.3}$$

where $\overline{T} = T - P$, the centrifugal forces are

$$T = \Omega^2\int_x^R m\tilde{x}\,\mathrm{d}\tilde{x}, \qquad \underline{T_t = \Omega^2\int_x^R m_t\tilde{x}\,\mathrm{d}\tilde{x}}, \tag{A.4}$$

and the external loadings and vibratory inertia loads obtained by D'Alembert's principle are [15]

$$p_y = L_y - m(\ddot{v} - e\ddot{\phi}\sin\beta) \tag{A.5a}$$

$$p_z = L_z - m(\ddot{w} + e\ddot{\phi}\cos\beta) \tag{A.5b}$$

$$q = M + me(\ddot{v}\sin\beta - \ddot{w}\cos\beta) - mk_m^2\ddot{\phi} \tag{A.5c}$$

$$\underline{p_{v_t} = -m_t\ddot{v}_t} \tag{A.5d}$$

$$\underline{p_{w_t} = -m_t\ddot{w}_t} \tag{A.5e}$$

Submitting Eqs. (A.2) and (A.3) into Eq. (A.1), integrating by parts and separating the variables yields the following partial differential equations

$$\left\{[EI_1\cos^2\beta + EI_2\sin^2\beta]w'' + [EI_2 - EI_1]\sin\beta\cos\beta v'' - \overline{T}e_A\phi\cos\beta - EB_2\beta'\phi'\sin\beta\right\}'' \\ - \left\{\overline{T}w' + \Omega^2 mxe\phi\cos\beta\right\}' - \left\{\overline{T}e_A\sin\beta\right\}'' - \left\{\Omega^2 mxe\sin\beta\right\}' + p_z = 0, \tag{A.6a}$$

$$\left\{[EI_1\sin^2\beta + EI_2\cos^2\beta]v'' + [EI_2 - EI_1]\cos\beta\sin\beta w'' + \overline{T}e_A\phi\sin\beta - EB_2\beta'\phi'\cos\beta\right\}''$$
$$- \left\{\overline{T}v' - \Omega^2 mxe\phi\sin\beta\right\}' + \Omega^2 me\phi\sin\beta - \left\{\overline{T}e_A\cos\beta\right\}''$$
$$- \left\{\Omega^2 mxe\cos\beta\right\}' - \Omega^2 m(e_0 + e\cos\beta) + p_y = 0, \quad \text{(A.6b)}$$

$$- \left\{\left[GJ + \overline{T}k_A^2 + EB_1\beta'^2\right]\phi' - EB_2\beta'[v''\cos\beta + w''\sin\beta]\right\}' + \overline{T}e_A(v''\sin\beta - w''\cos\beta)$$
$$+ \Omega^2 mxe(w'\cos\beta - v'\sin\beta) + \Omega^2 mev\sin\beta + \Omega^2 m\left[(k_{m2}^2 - k_{m1}^2)\cos 2\beta + ee_0\cos\beta\right]\phi$$
$$- \left\{\overline{T}k_A^2\beta'\right\}' + \Omega^2 m\left[(k_{m2}^2 - k_{m1}^2)\sin\beta\cos\beta + ee_0\sin\beta\right] + q = 0, \quad \text{(A.6c)}$$

$$(Pw_t')' + (T_t w_t')' + p_{w_t} = 0, \quad \text{(A.6d)}$$

$$(Pv_t')' + (T_t v_t')' + \Omega^2 m_t v_t + p_{v_t} = 0 \quad \text{(A.6e)}$$

and the boundary conditions

$$\delta w\{-(EI_1\cos\beta^2 + EI_2\sin\beta^2)w'' - (EI_2 - EI_1)\sin\beta\cos\beta v'' + (\overline{T}e_A + EB_2\beta'\phi')\sin\beta + \overline{T}e_A\phi\cos\beta\}'$$
$$+ \overline{T}w' + \Omega^2 mex(\sin\beta + \phi\cos\beta)|_0^R = 0, \quad \text{(A.7a)}$$

$$\delta w'\{(EI_1\cos\beta^2 + EI_2\sin\beta^2)w'' + (EI_2 - EI_1)\sin\beta\cos\beta v''$$
$$- (\overline{T}e_A + EB_2\beta'\phi')\sin\beta - \overline{T}e_A\phi\cos\beta\}|_0^R = 0, \quad \text{(A.7b)}$$

$$\delta v\{\{-(EI_2 - EI_1)\sin\beta\cos\beta w'' - (EI_1\sin\beta^2 + EI_2\cos\beta^2)v'' + (\overline{T}e_A - EB_2\beta'\phi')\cos\beta - \overline{T}e_A\phi\sin\beta\}'$$
$$+ \overline{T}v' + \Omega^2 mex(\cos\beta + \phi\sin\beta)\}|_0^R = 0, \quad \text{(A.7c)}$$

$$\delta v'\{(EI_2 - EI_1)\sin\beta\cos\beta w'' + (EI_1\sin\beta^2 + EI_2\cos\beta^2)v''$$
$$- (\overline{T}e_A - EB_2\beta'\phi')\cos\beta + \overline{T}e_A\phi\sin\beta\}|_0^R = 0, \quad \text{(A.7d)}$$

$$\delta\phi\left\{\left[GJ + \overline{T}k_A^2 + EB_1\beta'^2\right]\phi' + \overline{T}k_A^2\beta' - EB_2\beta'(v''\cos\beta + w''\sin\beta)\right\}|_0^R = 0, \quad \text{(A.7e)}$$

$$\delta w_t\left\{Pw_t' - T_t w_t'\right\}|_0^R = 0, \quad \text{(A.7f)}$$

$$\delta v_t\left\{Pv_t' - T_t v_t'\right\}|_0^R = 0. \quad \text{(A.7g)}$$

In order to separate the boundary conditions at the free and fixed end, the usual logic is used [6], i.e. the variation of displacements and slopes is zero at the fixed end and arbitrary at the free end. The former leads to the well known conditions for the fixed end (for $x = 0$)

$$w = w' = v = v' = \phi = w_t = v_t = 0, \quad \text{(A.8)}$$

while the latter requires the expressions in the curly brackets in Eq. (A.7) to be equal to zero, i.e. for $x = R$

$$\{-(EI_1\cos\beta^2 + EI_2\sin\beta^2)w'' - (EI_2 - EI_1)\sin\beta\cos\beta v'' + (EB_2\beta'\phi' - Pe_A)\sin\beta - Pe_A\phi\cos\beta\}'$$
$$- Pw' + \Omega^2 meR(\sin\beta + \phi\cos\beta) = 0, \quad \text{(A.9a)}$$

$$(EI_1\cos\beta^2 + EI_2\sin\beta^2)w'' + (EI_2 - EI_1)\sin\beta\cos\beta v'' + (Pe_A + EB_2\beta'\phi')\sin\beta + Pe_A\phi\cos\beta = 0, \quad \text{(A.9b)}$$

$$\{-(EI_2 - EI_1)\sin\beta\cos\beta w'' - (EI_1\sin\beta^2 + EI_2\cos\beta^2)v'' - (Pe_A + EB_2\beta'\phi')\cos\beta + Pe_A\phi\sin\beta\}' - Pv' + \Omega^2 meR(\cos\beta + \phi\sin\beta) = 0, \quad \text{(A.9c)}$$

$$(EI_2 - EI_1)\sin\beta\cos\beta w'' + (EI_1\sin\beta^2 + EI_2\cos\beta^2)v'' + (Pe_A + EB_2\beta'\phi')\cos\beta - Pe_A\phi\sin\beta = 0, \quad \text{(A.9d)}$$

$$\left[GJ - Pk_A^2 + EB_1\beta'^2\right]\phi' - Pk_A^2\beta' - EB_2\beta'(v''\cos\beta + w''\sin\beta) = 0, \quad \text{(A.9e)}$$

$$Pw_t' = 0, \quad \text{(A.9f)}$$

$$Pv_t' = 0. \quad \text{(A.9g)}$$

Equations (A.9a) and (A.9c) describe the shear effects at the tip of the beam. Equations (A.9b), (A.9d) and (A.9e) express the fact that there are no bending moments or torque applied at the tip, and Eqs. (A.9f) and (A.9g) describe the transversal forces at the end of the tendon.

In these boundary conditions, however, the important coupling between the tendon and the beam that is realised through the tip attachment fixture and through which the tendon is excited has not been taken into account. In order to introduce this coupling, the suitable geometric and load continuity conditions are needed. The geometric coupling requires the equality of the displacements of the beam and the tendon at the free end

$$w_{\mathrm{t}}(t,R) = w(t,R) + e_A(\sin\beta + \phi(t,R)\cos\beta), \quad \text{(A.10a)}$$

$$v_{\mathrm{t}}(t,R) = v(t,R) + e_A(\cos\beta - \phi(t,R)\sin\beta). \quad \text{(A.10b)}$$

The load equilibrium is then enforced by combining the boundary conditions in Eqs. (A.9f) and (A.9g), which can be interpreted as the tendon-induced cross-sectional shear forces acting at the tip of the beam, with the shear conditions in Eqs. (A.9a) and (A.9c). The new shear equilibrium conditions (A.9a) and (A.9c) therefore become

$$\{-(EI_1\cos\beta^2 + EI_2\sin\beta^2)w'' - (EI_2 - EI_1)\sin\beta\cos\beta v'' + (EB_2\beta'\phi' - Pe_A)\sin\beta - Pe_A\phi\cos\beta\}' - Pw' + \Omega^2 meR(\sin\beta + \phi\cos\beta) + Pw_t' = 0, \quad \text{(A.11a)}$$

$$\{-(EI_2 - EI_1)\sin\beta\cos\beta w'' - (EI_1\sin\beta^2 + EI_2\cos\beta^2)v'' - (Pe_A + EB_2\beta'\phi')\cos\beta + Pe_A\phi\sin\beta\}' - Pv' + \Omega^2 meR(\cos\beta + \phi\sin\beta) + Pv_t' = 0. \quad \text{(A.11b)}$$

In order to obtain the final set of boundary conditions, Eqs. (A.9f) and (A.9g) are replaced by Eqs. (A.10a) and (A.10b), leading to the set of BCs given by Eqs. (A.9b), (A.9d), (A.9e), (A.10) and (A.11). The final set of BCs is summarised and discussed in section 2.1.

Appendix B. Boundary value problem solver (bvp4c)

A solution of a boundary value problem can be conveniently found using a Matlab bvp4c solver [39]. It solves a system of first-order ordinary differential equations (ODEs)

$$\frac{\mathrm{d}y}{\mathrm{d}x} = f(x,y,p), \quad \text{for} \quad x_1 \le x \le x_2, \quad \text{(B.1)}$$

where x is an independent spatial variable, y is a vector of dependent variables, p is a vector of unknown parameters, and x_1 and x_2 are the boundary points. The system is accompanied by two-point boundary conditions

$$g(y(x_1), y(x_2), p) = 0. \quad \text{(B.2)}$$

The solver uses a finite difference code that implements the three-stage collocation Lobatto IIIa formula, and mesh selection and error control are based on the residual of the continuous solution [31]. This solver

is very versatile as it allows solutions of a wide range of boundary value problems to be found. However, it may suffer from a decreased numerical performance if an appropriate starting guess is not provided.

In order to evaluate the modal properties using a Matlab build-in bvp4c solver, an assumption of the normal mode must be used. A solution of any given dependent variable is expressed as the multiplication of the time-invariant mode shape and the time-varying harmonic function at the constant frequency in the following form

$$\begin{gathered} w(t,x) = W(x)\mathrm{e}^{\mathrm{i}\omega t}, \quad v(t,x) = V(x)\mathrm{e}^{\mathrm{i}\omega t}, \quad \phi(t,x) = \Phi(x)\mathrm{e}^{\mathrm{i}\omega t}, \\ w_{\mathrm{t}}(t,x) = W_{\mathrm{t}}(x)\mathrm{e}^{\mathrm{i}\omega t}, \quad v_{\mathrm{t}}(t,x) = V_{\mathrm{t}}(x)\mathrm{e}^{\mathrm{i}\omega t}, \end{gathered} \tag{B.3}$$

where ω is the natural frequency and $W(x), V(x), \Phi(x), W_t(x), V_t(x)$ are the components of the mode shape $\Phi(x)$ which represent, respectively, the bending in the z and y directions, the rotation about the elastic axis, and the transversal motion of the tendon in the z and y directions. Substituting the normal mode forms into the PDEs (Eq. (1)) allows one to eliminate time and rewrite the PDEs into a system of first order ODEs that, together with the BCs, define a boundary value problem. The final system consists of 14 first-order ODEs with 14 BCs. This boundary value problem can then be solved by a Matlab bvp4c solver for a single unknown natural frequency ω and the corresponding mode shape $\Psi(x)$ provided that the appropriate starting guess consisting of the natural frequency and mode shape is provided. The accuracy of the starting guess is crucial for the successful solution. The initial natural frequency and the mode shape can be either obtained from a harmonic response of the system, or by using the differential quadrature method (DQM) as described in section 2.2.

Appendix C. Differential quadrature method (DQM)

In order to discretise the partial differential equations using the differential quadrature method (DQM), the domain x must be firstly sampled into N_x points. Usually Chebyshev-Gauss-Lobatto point distribution

$$x_i = \frac{R}{2}\left[1 - \cos\frac{\pi(i-1)}{N_x - 1}\right] \tag{C.1}$$

is used for its good numerical properties. In addition, for the present system of the fourth-order PDEs a δ-point technique [32] must be used to add two more sampling points close to the boundaries of the domain. These points are used to approximately evaluate two boundary conditions at each end. Secondly, the derivatives of unknown functions at a specific domain coordinate are approximated by the weighted linear combinations of the functional values at all other sampling points along the domain, i.e.

$$\begin{gathered} w' = \sum_{j=1}^{N} A_{ij}^{(1)} w_j, \quad w'' = \sum_{j=1}^{N} A_{ij}^{(2)} w_j, \quad w''' = \sum_{j=1}^{N} A_{ij}^{(3)} w_j, \quad w'''' = \sum_{j=1}^{N} A_{ij}^{(4)} w_j, \quad v' = \sum_{j=1}^{N} A_{ij}^{(1)} v_j, \\ v'' = \sum_{j=1}^{N} A_{ij}^{(2)} v_j, \quad v''' = \sum_{j=1}^{N} A_{ij}^{(3)} v_j, \quad v'''' = \sum_{j=1}^{N} A_{ij}^{(4)} v_j, \quad \phi' = \sum_{j=1}^{N} A_{ij}^{(1)} \phi_j, \quad \phi'' = \sum_{j=1}^{N} A_{ij}^{(2)} \phi_j, \\ w_t' = \sum_{j=1}^{N} A_{ij}^{(1)} w_{tj}, \quad w_t'' = \sum_{j=1}^{N} A_{ij}^{(2)} w_{tj}, \quad v_t' = \sum_{j=1}^{N} A_{ij}^{(1)} v_{tj}, \quad v_t'' = \sum_{j=1}^{N} A_{ij}^{(2)} v_{tj}, \end{gathered} \tag{C.2}$$

where the weighting coefficients $A_{ik}^{(r)}$ can be computed in various ways. However, it is known that the formulas developed in [32] provide very accurate results and good numerical properties. The off-diagonal terms of the first derivative are given by

$$A_{ik}^{(1)} = \frac{\Pi(x_i)}{(x_i - x_k)\Pi(x_k)}, \quad \text{for} \quad i,k = 1,2,\ldots,N_x \quad \text{and} \quad k \neq i \tag{C.3}$$

where

$$\Pi(x_i) = \prod_{\upsilon=1,\upsilon\neq i}^{N_x} (x_i - x_\upsilon) \quad \text{and} \quad \Pi(x_k) = \prod_{\upsilon=1,\upsilon\neq k}^{N_x} (x_k - x_\upsilon) \tag{C.4}$$

and the higher-order derivatives are obtained using the following recurrence relationship

$$A_{ik}^{(r)} = r\left[A_{ii}^{(r-1)}A_{ik}^{(1)} - \frac{A_{ik}^{(r-1)}}{x_i - x_k}\right] \quad \text{for} \quad i,k = 1,2,\ldots,N_x, \quad k \neq i, \quad \text{and} \quad r \in [2, N_x - 1]. \tag{C.5}$$

The missing diagonal terms of the weighting matrices are evaluated using

$$A_{ii}^{(r)} = -\sum_{v=1, v\neq i}^{N_x} A_{iv}^{(r)} \quad \text{for} \quad i = 1,2,\ldots,N_x. \tag{C.6}$$

The system of PDEs in Eq. (1) and the BCs in Eqs. (3) and (4) can be re-written using Eq. (C.2) to the following form

$$\mathcal{M}\ddot{\mathbf{U}} + \mathcal{K}\mathbf{U} = \mathcal{F}, \tag{C.7}$$

where

$$\mathbf{U} = [w_1, \ldots, w_{N_x}, v_1, \ldots, v_{N_x}, \phi_1, \ldots, \phi_{N_x}, w_{t1}, \ldots, w_{tN_x}, v_{t1}, \ldots, v_{tN_x}]^T \tag{C.8}$$

is a vector of all unknown functional values in all sampling points. All the spatial derivatives have been removed, but the boundary conditions are still included in the systems and must be eliminated. In order to eliminate the boundary conditions, the following partition is required

$$\mathbf{U} = [\mathbf{U}_b, \mathbf{U}_d]^T, \tag{C.9}$$

where

$$\mathbf{U}_b = [w_1, w_2, w_{N_x-1}, w_{N_x}, v_1, v_2, v_{N_x-1}, v_{N_x}, \phi_1, \phi_{N_x}, w_{t1}, w_{tN_x}, v_{t1}, v_{tN_x}]^T, \tag{C.10}$$

and

$$\mathbf{U}_d = [w_3, \ldots, w_{N_x-2}, v_3, \ldots, v_{N_x-2}, \phi_2, \ldots, \phi_{N_x-1}, w_{t2}, \ldots, w_{tN_x-1}, v_{t2}, \ldots, v_{tN_x-1}]^T. \tag{C.11}$$

Then, the system from Eq. (C.7) becomes

$$\begin{bmatrix} \mathbf{0} & \mathbf{0} \\ \mathbf{0} & \mathbf{M}_{dd} \end{bmatrix} \begin{bmatrix} \ddot{\mathbf{U}}_b \\ \ddot{\mathbf{U}}_d \end{bmatrix} + \begin{bmatrix} \mathbf{K}_{bb} & \mathbf{K}_{bd} \\ \mathbf{K}_{db} & \mathbf{K}_{dd} \end{bmatrix} \begin{bmatrix} \mathbf{U}_b \\ \mathbf{U}_d \end{bmatrix} = \begin{bmatrix} \mathbf{F}_b \\ \mathbf{F}_d \end{bmatrix} \tag{C.12}$$

or

$$\mathbf{K}_{bb}\mathbf{U}_b + \mathbf{K}_{bd}\mathbf{U}_d = \mathbf{F}_b, \tag{C.13a}$$

$$\mathbf{M}_{dd}\ddot{\mathbf{U}}_d + \mathbf{K}_{db}\mathbf{U}_b + \mathbf{K}_{dd}\mathbf{U}_d = \mathbf{F}_d. \tag{C.13b}$$

From Eq. (C.13a), $\mathbf{U}_b$ can be obtained as

$$\mathbf{U}_b = \mathbf{K}_{bb}^{-1}(\mathbf{F}_b - \mathbf{K}_{bd}\mathbf{U}_d) \tag{C.14}$$

and by submitting this expression to Eq. (C.13b), the final set of ODEs is obtained as

$$\underbrace{\mathbf{M}_{dd}}_{\mathbf{M}}\ddot{\mathbf{U}}_d + \underbrace{(\mathbf{K}_{dd} - \mathbf{K}_{db}\mathbf{K}_{bb}^{-1}\mathbf{K}_{bd})}_{\mathbf{K}}\mathbf{U}_d = \underbrace{\mathbf{F}_d - \mathbf{K}_{db}\mathbf{K}_{bb}^{-1}\mathbf{F}_b}_{\mathbf{F}}, \tag{C.15}$$

where $\mathbf{K}$ is an equivalent stiffness matrix that respects the boundary conditions, $\mathbf{M}$ is a mass matrix, and $\mathbf{F}$ is a vector of external excitation forces. Since Eq. (C.15) is a set of ODEs in the standard form, any conventional analysis, such as the modal analysis used in this paper, can be applied to the obtained structural matrices to evaluate $\mathbf{U}_d$. Corresponding values at the boundaries can then be computed from Eq. (C.14) if required.